International Journal of Fatigue 134 (2020) 105466

Contents lists available at ScienceDirect

International Journal of Fatigue

journal homepage: www.elsevier.com/locate/ijfatigue

Study of the biaxial fatigue behaviour and overloads on S355 low carbon steel

A.S. Cruces[a], M. Mokhtarishirazabad[a,b], B. Moreno[a], M. Zanganeh[c], P. Lopez-Crespo[a,*]

[a] Department of Civil and Materials Engineering, University of Malaga, C/Dr Ortiz Ramos s/n, 29071 Málaga, Spain
[b] Department of Mechanical Engineering, University of Bristol, Bristol, UK
[c] NASA Johnson Space Center, Houston, TX, USA

ARTICLE INFO

Keywords:
Biaxial fatigue
Overload
Critical plane methods
COD
Effective stress intensity factor

ABSTRACT

This work aimed to study the fatigue behaviour of S355 low carbon steel under uniaxial and biaxial loading conditions and to measure the overload effects under both types of loads. The analysis is performed with a local strain approach and with damage tolerance approach. Local strain based investigation was based on Fatemi-Socie critical plane model. This allows the life reduction caused by growing the crack from a stress raiser to be quantified. The fatigue life reduction caused by applying simultaneously torsional and tension loads was also evaluated with Fatemi-Socie model. In addition, the crack opening displacement (COD) and the effective stress intensity factor (SIF) were evaluated experimentally via full-field technique of digital image correlation (DIC). Both COD and SIF have been useful to understand the transient effects caused by a 40% overload under the two types of load. In addition, COD measurements allowed the offset compliance method for evaluating the opening load to be applied on a cylindrical specimen subjected to tension load. SIF estimation was also useful to quantify the mode mixity (I + II) developed during the experiment under the two types of load.

1. Introduction

Multiaxial and biaxial loading conditions can reduce drastically the life of mechanical components compared to uniaxial loading [1]. Multiaxial and biaxial research tends to be based on the local strain approach. For example, stress invariant method has been useful to predict the behaviour under multiaxial conditions from a local strain approach life point of view [2]. This early work showed the relation between that failure and the mean stress, the alternating parts of the cyclic stress components and their time shifts. Also within the family of local strain approach, Sonsino and Grubisic predicted the fatigue life under combined in-phase and out-of-phase axial and shear strains [3]. Based on the use of space averages of strain components, they were able to understand the out-of-phase life reduction on a cyclically softening steel and on a cyclically hardening steel. In addition, critical plane model theories are also based on the local strain approach, with Fatemi-Socie damage parameter being probably the most versatile model for a range of materials and conditions [4]. The original work performed on Inconel 718 allowed out-of-phase multiaxial loading to be identified as a cause for additional cyclic hardening. Moreover, energy concepts were also invoked within the local strain approach in an attempt to integrate the path dependence of the fatigue process [5]. Such approach combined with the use of multiaxial constraint factor proved to be successful for different strain ratios and specimen geometries [6].

Besides local strain approach, fatigue crack growth analysis based on the damage tolerant approach has also been used for structures prone to linear elastic failure. The stress intensity factor (SIF) is known as one of the most important fracture parameters for characterising the fatigue crack growth behaviour of engineering components. Since 1957 when Irwin [7] formulised the stress intensity factor, a considerable work has been done to improve our understanding on its importance in crack growth behaviour under static and cyclic loading [8,9]. Finite element method has been employed widely during last decades for detailed analysis of the crack tip fields (stress, strain, displacement) to evaluate the SIF and phenomenon such as crack closure [10–12]. In addition, some mathematical models have been introduced describing the crack tip field such as Westergaard's [13], Williams' [14], Muskhelishvili's [15], and recently CJP [16] models. Different techniques have been developed to measure full-field experimental information around the crack tip, such as Moiré interferometry [12], photo-elasticity [17], thermo-elasticity [18], digital image correlation (DIC) [19] and synchrotron X-ray diffraction [20]. Among these techniques, DIC is widely used due to a number of advantages such as being easy to implement, easy sample preparation, and being a scale-free method. The

* Corresponding author.
E-mail address: plopezcrespo@uma.es (P. Lopez-Crespo).

https://doi.org/10.1016/j.ijfatigue.2019.105466
Received 4 June 2019; Received in revised form 11 November 2019; Accepted 31 December 2019
Available online 02 January 2020

latter one means that it can measure on the scale ranging from a few meters [21] to micro-meters [22,23]. Measured displacement data by DIC can be fitted to one of abovementioned models using the multi-point over-deterministic (MPOD) method [24] to estimate the SIF [19,25,26].

In order to estimate the fatigue life under variable amplitude loading conditions, it is essential to quantify the crack growth rate, which is in turn, affected by the plastic deformation at the crack tip. The effect of external load variation on the crack growth rate is often studied by investigating the effects of a single overload [27,28]. Nowell et al. [12] employed Moiré interferometry and DIC to determine the presence of crack closure in propagating fatigue crack by examining the measured in-plane displacement around the crack tip. They used a similar method used previously by de Matos [29] to monitor the displacement of some pairs of points close to the crack tip for determining the closure level. DIC was also used by Yusof et al. [30] to determine the closure load using crack opening displacement (COD) and evaluated SIF. They used Muskhilishvili's model to evaluate the experimental SIF. Others have conducted experimental and numerical investigation on the effect of an overload cycle on fatigue crack growth under mixed mode loading [31–33]. Nevertheless, the knowledge regarding the application of optical methods to study the effect of overload cycle on the crack growth rate under tension-tension (uniaxial) and tension-torsion (biaxial) cyclic loading is very limited.

This work presents a comprehensive study on S355 steel combining local strain and damage tolerant approaches. The local strain approach analysis is performed with Fatemi-Socie critical plane method [4]. Critical plane methods are very useful to predict not only the fatigue life but also the failure plane [34]. This second element is very important because it can determine whether a defect is critical or not, along with the component geometry and the type of load. Fatigue crack growth analysis is complemented with DIC experimental evaluation of the COD and the effective SIF via MPOD method [24] to study the overload retardation, the effect of closure and the existence of mixed-mode cracking.

2. Description of the fatigue experiments

The experiments are conducted on a low carbon S355 steel (also know as St52-3N). Due to its good weldability and high ductility, this alloy is often used in offshore platforms and marine structures. Table 1 shows the chemical composition of the material. The mechanical behaviour of the alloy is showed in Table 2. This material combines very good fatigue properties with low environmental impact for non-transport applications [35].

The microstructure of the alloy consists of ferrite and pearlite bands as vertical white and black bands, respectively (Fig. 1). The experiments were developed on dog bone shaped cylindrical specimens. Fig. 2 illustrates a schematic of the geometry.

Axial and biaxial loads under load control mode were conducted by a MTS 809 servo-hydraulic loading rig coupled by a biaxial extensometer Epsilon 3550. Uniaxial tension-tension cyclic loading tests were conducted on four specimens, namely U1, U2, U3 and U4, with sinus signal and axial load ratio of 0.1 ($R_a = 0.1$). The U refers to uniaxial loading (see nomenclature in Table 3). Additionally, four other specimens, namely B1, B2, B3 and B4 were subjected to biaxial loading (in-phase torsional load with load ratio of -1 ($R_t = -1$) superimposed to the axial loadings). The range of axial load was 0.56 of the yielding strength of the alloy. Fig. 3 shows the loading path for the biaxial

Table 1
Chemical composition in S355 steel. The balance is Fe.

C	Si	Mn	Si	P	S	Cr	Ni	Mo
0.17	0.225	1.235	0.225	0.01	> 0.0001	0.07	0.06	0.016

Table 2
Monotonic properties of S355 steel.

Property	Value
Yield strength, σ_y	386 MPa
Ultimate strength, σ_u	639 MPa
Young's Modulus, E	206 GPa
Shear Modulus, G	78 GPa

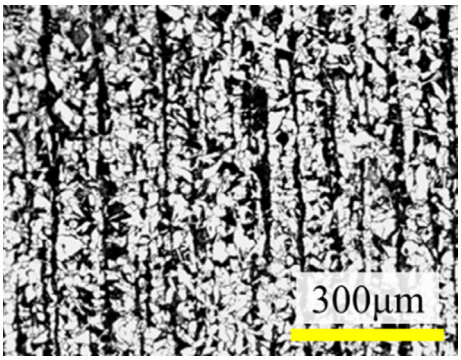

Fig. 1. The microstructure of S355 steel. Black and white vertical bands are showing the pearlite and ferrite bands, respectively.

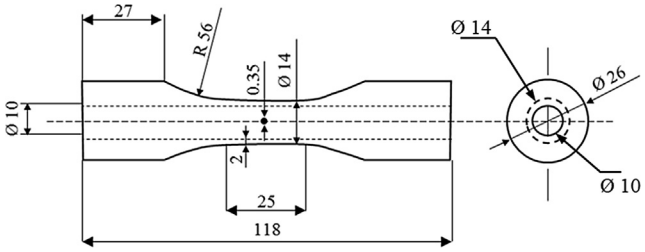

Fig. 2. The geometry of the hollow cylinder specimen with a central hole. All dimensions are in mm.

Table 3
Axial and shear stress values for specimens with and without overload cycle.

Specimens	Load type	OL in the test	Crack length at OL, µm	Δσ MPa	Δτ MPa	$\Delta\sigma_{OL}$ MPa	$\Delta\tau_{OL}$ MPa
U1, U2	Uniaxial	No	–	216	–	302	–
U3, U4	Uniaxial	Yes	1.98				
B1, B2	Biaxial	No	–	216	277	302	388
B3, B4	Biaxial	Yes	1.58	216	277	302	388

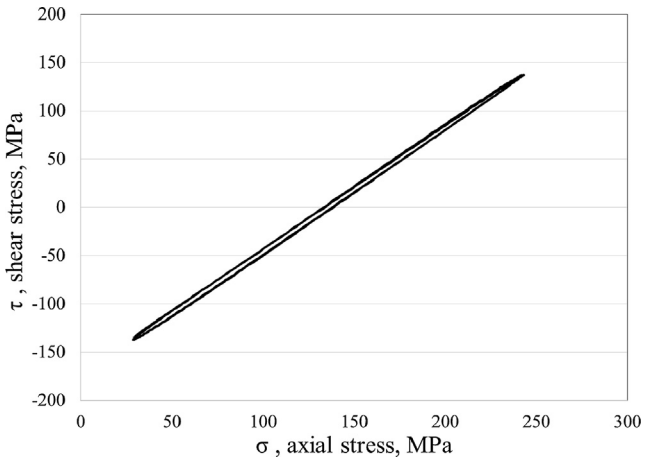

Fig. 3. Loading path for samples B.

loading. To enforce the crack to nucleate inside the field of view imaged by the optical system, through holes with diameters ranging between 0.38 and 0.47 mm were drilled in the outer surface of all specimens. Drill bits of 0.3 mm diameter were used in all the cases. A small drill (Dremel MultiPro, 130 W) that could support such small bits was used. The hole was introduced in around 10 steps, with low speed of progression and a turning speed of the drill of 10,000 rpm. In addition, in order to avoid breaking the bit too much, it was required to clean the bit every few steps, removing the metal chips created during the previous steps and adding some oil to the bit to avoid extra heating and improve lubrication. Introducing the holes was very challenging experimentally. Nevertheless, we believe the difference in hole diameter did not affect much the fatigue behaviour, since in other specimens the crack appeared at locations different to the hole. The crack length was determined by adding the radius of drilled hole to the length of the crack from the crack initiation point at the circumference of the hole to the crack tip in one side of the hole. The crack length on both sides of the hole was the very similar. Up to 39 μm difference on either side of the crack was measured at different stages during the experiments. Such small differences are attributed to microstructural influence. The end of test was limited by the optical setup employed. When the crack length was larger than ~1.6 mm on either side of the hole, the crack tip moved outside the field of view employed for tracking the tip and measuring the displacement field. Readjusting the optical setup position was not possible due to the difficulty of maintaining the same working distance before and after readjustment. Accordingly, end of test was limited to ~3 mm, which also agrees well with damage tolerant approach, where tolerable flaw size should be such that fatigue crack growth is relatively small [9].

In order to study the effect of the overload on the crack propagation behaviour, a 40% overload was applied on half of the samples. The overload was applied when the crack length was approximately 1.98 mm in the uniaxial samples U and 1.58 mm in the biaxial samples. The mechanisms controlling the propagation for both crack lengths are the same, since the crack length in both cases is considerably larger than the microstructural size [36]. The load range in the overload cycle was 1.4 times larger than load range during the rest of the test. The effect of overloads on short crack subjected to biaxial loading was not study here. The mechanisms controlling the propagation are different for short cracks and cannot be described accurately by LEFM. The cyclic loading then continued until the crack length reached ~3 mm. Table 3 shows the loads applied on the different samples. The crack length was evaluated from the crack-tip position with optical microscopy. The average error in measuring the crack growth rate was 0.002 μm/cycle. The incremental polynominal technique, as recommended by ASTM E647-15 [37], was employed to examine the cyclic crack growth rate.

3. Image acquisition and image processing

Crack tip displacement fields were captured during cyclic loading with a 5 MP CCD camera coupled with a macro Navitar lens and adaptor tube which provided a field of view (FOV) was $3.55 \times 2.97\ mm^2$. The contrast required for DIC technique was introduced by finely abrading the surface so that the bare crack tip region is imaged directly [38]. This allowed faster and easier positioning of the crack tip [39]. In this way, a resolution of 1.45 μm per pixel was obtained. The arithmetic average surface roughness *Ra* was 0.4 μm, that is around half the roughness required for measuring fatigue crack growth rates according to ASTM [40]. In order to allow sufficient number of images to be acquired during each cycle, the loading frequency was reduced from 3 Hz to 0.3 Hz. This allowed around 75 images to be captured during a complete cycle. The digital images were processed by VIC 2D V6 software in order to obtain displacement fields [41]. Recommendations given in [42] were followed to improve the quality of the SIF estimations. Accordingly, a high order interpolation scheme of optimized 8-tap spline was used for DIC analysis to achieve sub-pixel accuracy. The subset size was adjusted to 39 × 39 pixels. In addition, only 25% of the crack line was considered in the area of interest (the area where the displacement data were measured by DIC). The relative error in the estimated displacement (and consequently in COD) was 2.95%. This relative error was estimated from the quality of the correlation of the images taken at different loads.

4. Study with Fatemi-Socie model

The analysis consists of evaluating the damage in different planes and choosing the plane where a maximum damage occurs, namely the critical plane [34]. The location of the critical plane changes depending on the fatigue stage, the type of material and the loading conditions [43]. For ductile materials, the dominant failure plane favours maximising the shear strain or mode II/III strain. For brittle materials the dominant failure plane favours maximising the normal strain or mode I strain. Fatemi-Socie critical plane model is used here to estimate the fatigue life and the failure plane for the two samples [4]. Fatemi-Socie model was chosen because it has proven to generate good predictions on S355 steel under few different loading conditions [44].

Fatemi-Socie model is an equivalent strain type of model and is based on mode II/III failure. The critical plane is defined from the plane where the shear strain is maximum. In addition, it includes the mean stress effect through the maximum value of the normal stress on the critical plane. The model is summarised according to Eq. (1):

$$\frac{\Delta\gamma_{max}}{2}\left(1 + k\frac{\sigma_{n,max}}{\sigma_y}\right) = \frac{\tau'_f}{G}(2N_f)^{b_\gamma} + \gamma'_f(2N_f)^{c_\gamma} \quad (1)$$

where $\Delta\gamma_{max}/2$ is the maximum shear strain amplitude, $\sigma_{n,max}$ is the maximum tensile stress at the critical plane, σ_y is the yield stress, G is the shear modulus, τ'_f is the shear fatigue strength coefficient, b_γ is the shear fatigue strength exponent, γ'_f is the shear fatigue ductility coefficient and c_γ is the shear fatigue ductility exponent and k is a parameter that weight the normal stress effect on the critical plane.

k parameter is a correction factor that relates the shear strain that appear in a pure torsion test and the maximum shear strains that appear in a tension-compression test. The values for k parameter is defined as a function of the fatigue life, N_f, according to equation (2) [34].

$$k = \left[\frac{\frac{\tau'_f}{G}(2N_f)^{b_\gamma} + \gamma'_f(2N_f)^{c_\gamma}}{(1+\nu_e)\frac{\sigma'_f}{E}(2N_f)^{b} + (1+\nu_p)\varepsilon'_f(2N_f)^{c}} - 1\right]\frac{\sigma'_y}{\sigma'_f(2N_f)^{b}} \quad (2)$$

where E is the Young modulus and G is the shear modulus. All other properties used in Eq. (2) are given in Table 4.

The drill generates a stress concentrator, which increases considerably the stress/strain values thereby reducing the total fatigue life. The stress/strain values produced by the drill were estimated with a Finite Element Model (FEM) implemented with Ansys [45]. The symmetry in the geometry and the loads in the uniaxial specimen (samples

Table 4
Tensional and torsional mechanical properties used to evaluate the correction factor, k, in Fatemi-Socie model.

Property	Value
Poisson's ratio in the elastic regime, ν_e	0.3
Poisson's ratio in the plastic regime, ν_p	0.5
Cyclic yield strength, σ'_y	321.3 MPa
Fatigue strength coefficient, σ'_f	564.4 MPa
Fatigue strength exponent, b	−0.0576
Fatigue ductility coefficient, ε'_f	0.1554
Fatigue ductility exponent, c	−0.4658
Fatigue torsional strength coefficient, τ'_f	486.9 MPa
Fatigue torsional strength exponent, b_γ	−0.0668
Fatigue torsional ductility coefficient, γ'_f	0.0662
Fatigue torsional ductility exponent, c_γ	−0.3191

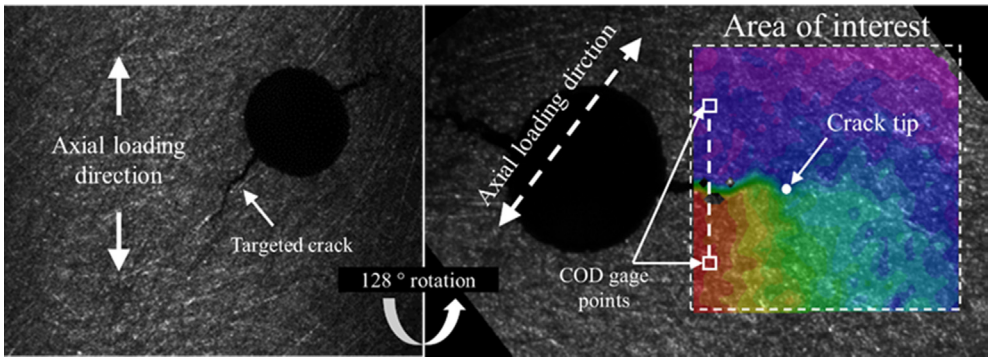

Fig. 4. The field of view of the sample B3 and the vertical displacement contour around the crack-tip derived by DIC. The image is rotated 128 degree counter clockwise to obtain a horizontal crack line. The position of COD gauge points is also illustrated.

U) allowed the model to be reduced to one fourth of the total geometry. It was not possible to implement the symmetry simplification for samples B because the applied loads were not symmetrical. 3489 tetrahedral elements were used in the model, with the smallest being 10 μm in the region surrounding the hole. Chaboche kinematic hardening model was employed Eq. (3) [46].

$$\dot{\alpha} = \frac{2}{3}\sum_{i=1}^{n} C_i \dot{\varepsilon}^{pl} - \gamma_i \alpha_i \dot{\lambda} \tag{3}$$

where α is the back stress, n is the number of kinematic models to use, C_i is the hardening modulus, γ_i is the rate of decrease of hardening, ε^{pl} is the plastic strain and λ is the accumulated plastic strain. The effect of isotropic hardening is included through the stress-strain curve, retrieved from the literature [47].

Fig. 5 shows the equivalent strain map for sample B3 after 20 cycles for the point with maximum normal stress and shear stress (see Fig. 3).

4.1. Fatigue life predictions

The fatigue life results for all samples are shown in Table 5 together with the predictions obtained by the Fatemi-Socie model. The overload described in Section 2 was introduced when the crack length was 1.98 for samples U3 and U4, and 1.58 mm for samples B3 and B4. That is the overload was introduced during the last stage of the test (less than 10% of fatigue life remaining). It is observed that introducing a shear component in the load drastically reduces the fatigue life, in agreement with previous works [48,49]. Table 5 also indicates that the overload increases the fatigue life with respect the non-overload conditions, both in the uniaxial and the biaxial loadings. In terms of percentage, the increment in life is around 30% and 80% on average for the uniaxial and biaxial conditions, respectively. However, these increments were around 300,000 and 10,000 cycles for the uniaxial and biaxial conditions, respectively.

Table 5
Fatigue lives measured experimentally ($N_{f\ exp}$) and predicted by the Fatemi-Socie model ($N_{f\ FS}$).

Specimen	$N_{f\ exp}$ (Cycles)	$N_{f\ FS}$ (Cycles)
U1	1.03×10^6	5.41×10^5
U2	9.18×10^5	5.41×10^5
U3	1.21×10^6	5.41×10^5
U4	1.33×10^6	5.41×10^5
B1	14,000	15,912
B2	13,000	15,912
B3	28,600	15,912
B4	20,250	15,912

The correction factor k (Eq. (2)) was 0.895 and 0.333 for samples U and samples B, respectively. The weight of the normal component in the correction factor increases as the fatigue life increases. The fatigue lives predicted are approximately half of the experimental fatigue lives, which is normally taken as satisfactory predictions [50,51]. In addition, the predictions are on the conservative side, similarly to previous works where Fatemi-Socie model was employed for estimating the fatigue life [52,53]. Ignoring the stress concentrator effect caused by the hole led to very inaccurate life predictions by the Fatemi-Socie model. Table 5 also indicates that the fatigue life reduction caused by shifting from uniaxial loading to biaxial loading is modelled correctly by Fatemi-Socie model.

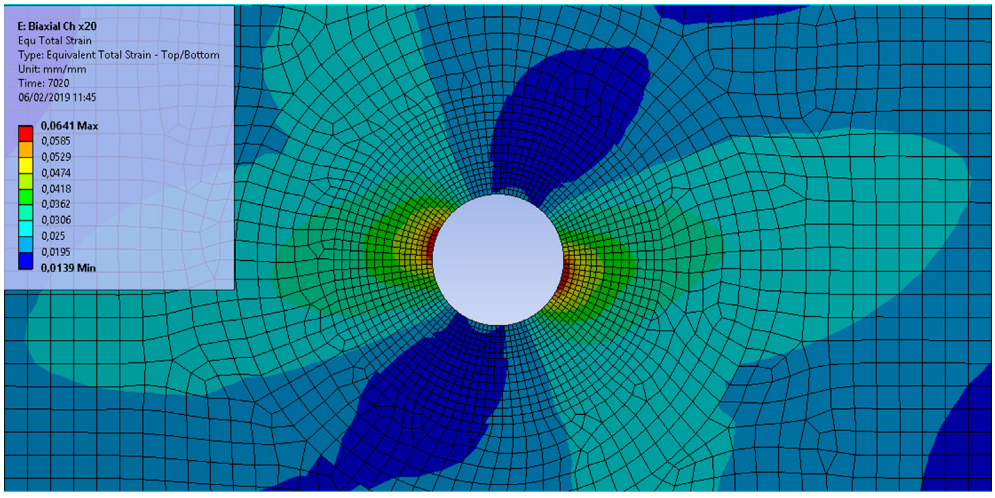

Fig. 5. Map of equivalent strain for sample B3 at maximum load after 20 cycles.

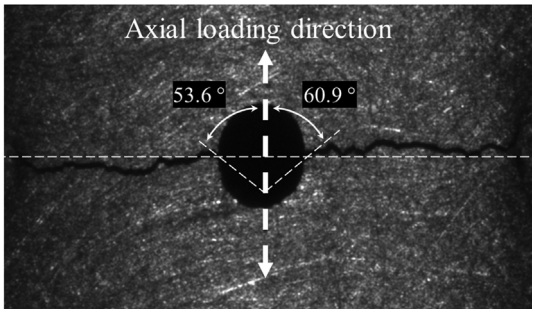

Fig. 6. Measurement of angles at initiation for sample U3.

4.2. Failure plane predictions

Fatemi-Socie critical plane model was also employed to investigate the failure plane. To this end, image processing software Image-J [54] was used to measure the initiation angle on all the samples. Fig. 6 shows the angles measured at initiation for sample U3. All angles were measured with respect the longitudinal direction of the sample (vertical axis in Fig. 6). The different loading condition was previously found to affect directly the initiation angle in structural steels [55].

The cracking angles at initiation measured experimentally and predicted by the Fatemi-Socie model are summarised in Table 6. For each sample, two different angles are shown in Table 6, relative to the crack initiated to the left hand side of the hole (Exp. angle 1) and the crack initiated to the right hand side of the hole (Exp. angle 2). Similar behaviour was previously observed on 2024-T3 aluminium alloy when it was subjected to axial and biaxial loads [56]. The predictions produced by the Fatemi-Socie model in the low cycle fatigue regime agree well with previous analysis on S355 steel [44]. Cracking angle measurements are often affected by microstructural barriers such as grain boundaries and different phases with different strengths (see Fig. 1) and strain hardening of the material surrounding the hole, thereby producing a large scattering. In addition, the Fatemi-Socie model is able to predict one particular angle based on the maximum value of the damage parameter (left hand side in Eq. (1)). Nevertheless, there is a large volume of material subjected to a damage parameter that is 90% of the maximum damage parameter. Such volume includes the angle predicted by the critical plane $\pm 18^{\circ}$ [44]. In around 62% of the samples the predictions were satisfactory, taking into account the $\pm 18^{\circ}$ angle.

5. Damage tolerant analysis

5.1. Fatigue crack growth rate analysis

Fig. 7 shows the evolution of crack growth rate for the different samples. Fig. 7.a shows the results under uniaxial load (samples U) and Fig. 7.b shows the results under biaxial load (samples B). The different positions of the curves in Fig. 7 is caused by the difference in the initiation of the crack. Fig. 7 also shows larger oscillations for the early stages of the crack motivated by the difficulty in identifying the crack tip for short cracks. This is particularly obvious for samples B1, B2 and B3 in Fig. 7. In order to compare the different curves, the fatigue life was corrected for the different samples for crack length and is shown in Fig. 8. There are some interesting differences between the crack behaviour under uniaxial and biaxial loading regimes. Fig. 8 shows that the crack growth rate is considerably higher (by a factor of about 20) for samples B than for samples U. This larger growth rate is caused by the superposition of in-phase torsional load to the axial cyclic load. By calculating the principal stresses, it was observed that the principal stress normal to the crack line (σ_1) and the equivalent von Mises stress (σ_e) at the maximum axial load for samples B were 303 and 338 MPa, respectively. That is 26% and 40% higher than applied axial load in samples U. It appears that the retardation produced by the overload is larger for the uniaxial samples (U3 and U4) than for the biaxial samples (B3 and B4). Fig. 8 shows that the duration of the retardation is notably larger for the uniaxial overloaded samples than for the biaxial overloaded samples (retardation of ~42,000 cycles in uniaxial and retardation of ~3500 cycles in biaxial). Such delay in retardation has been observed previously for biaxial loading where the range of baseline axial and shear stress was 25% and 17% lower than that of the biaxial samples [57]. Moreover, the distance advanced by the crack during the transient period after overload was 194 and 390 μm on average the uniaxial samples and the biaxial. That is, a longer retardation is observed in terms of cycles for the uniaxial samples, and a longer retardation is observed in terms of crack advance for the biaxial samples. This is probably related to the higher growth rate in the biaxial specimens.

Although the stress amplitude (σ_a) for the biaxial samples was almost the same as for the pure axial loading condition, the mean stress has been increased form 136 MPa in samples U to 231 MPa in samples B. The change in orientation of the principal axis with respect to the loading axis (θ) during a complete cycle indicates that samples B are subjected to non-proportional loading [58]. This can be seen more clearly in Fig. 9 where the evolution of the principal axis orientation (θ) is shown during two cycles for samples B. The orientation, θ, changes between -49 and 27°. Fig. 9 also shows the evolution of the nominal, principal and Von Mises equivalent stresses along two cycles. Although axial and torsional loads were in phase, the theta and σ/τ changed during each cycle of loading, thus making the loads being non-proportional. The higher values of stresses together with the more damaging effect of non-proportional loading compared to proportional loading [4] account for the faster propagation observed in samples B compared to samples U (see Table 5 and Fig. 8).

Table 6
Experimental angles measured at initiation and angle predicted by the Fatemi-Socie model (FS angle). Both experimental angles (crack growing towards the left hand side - Exp. angle 1, and crack growing towards right hand side - Exp. angle 2) are shown.

Specimen	Exp. angle 1	Exp. angle 2	FS angle
U1	55.9°	64.3°	40.0°
U2	45.0°	43.2°	40.0°
U3	53.6°	60.9°	40.0°
U4	49.3°	60.6°	40.0°
B1	30.3°	51.5°	65.0°
B2	56.4°	60.0°	65.0°
B3	36.6°	64.8°	65.0°
B4	65.4°	41.6°	65.0°

Table 7
Definition of fatigue stages for uniaxial, U, and biaxial, B, samples.

Cycles for samples U	Cycles for samples B	Fatigue stage
OL − 1 cycle	OL − 1 cycle	FS1
OL + 2 cycle	OL + 1 cycle	FS2
OL + 25 kcycle	OL + 3 kcycle	FS3
OL + 50 kcycle	OL + 4 kcycle	FS4

5.2. Crack opening displacement examination

The crack opening displacement (COD) was estimated from DIC measurements taken 0.3 mm behind the crack tip. The displacement data from above and below the crack line were used for computing the COD according to:

$$\mathrm{COD} = \sqrt{(u_{xbot} - u_{xtop})^2 + (u_{ybot} - u_{ytop})^2} \quad (4)$$

where u_x and u_y are the horizontal and vertical displacement respectively. The subscripts “top” and “bot” refer to the position (top and

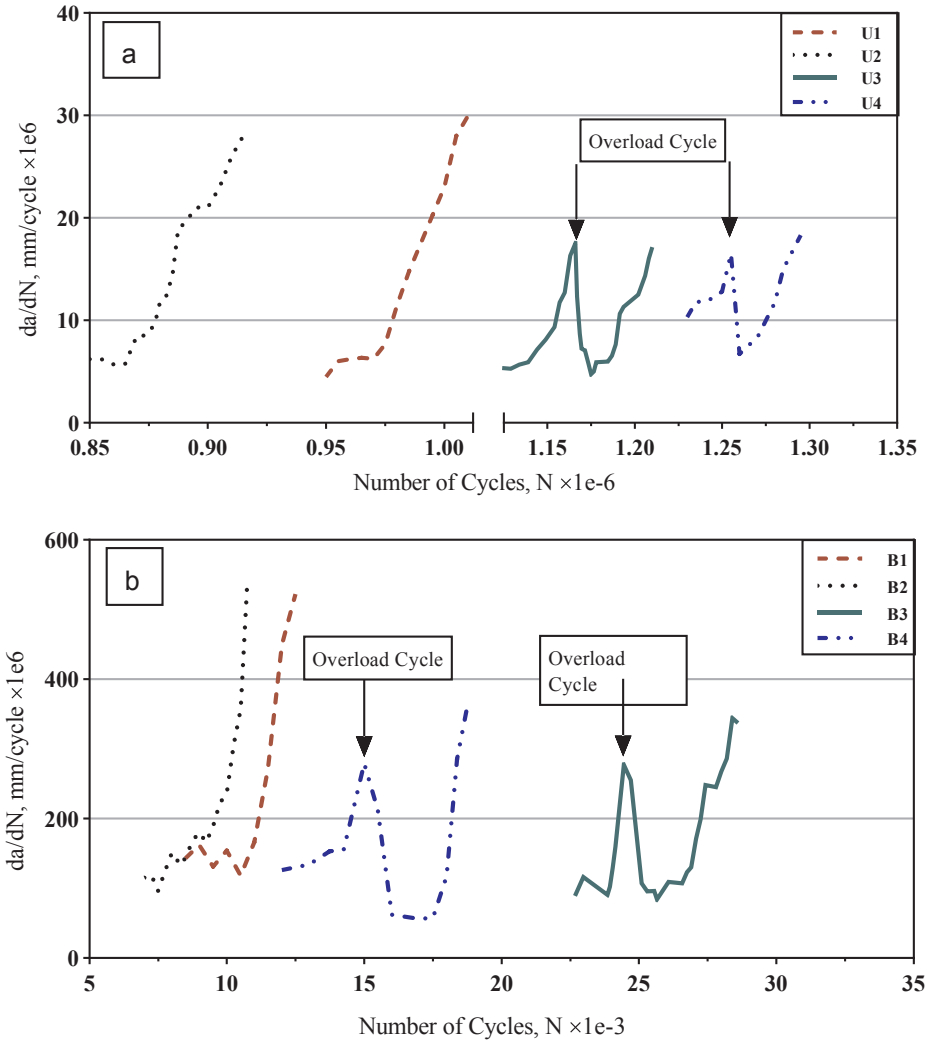

Fig. 7. Evolution of crack growth rate as a function of number of cycles for uniaxial (a) and biaxial (b) tests.

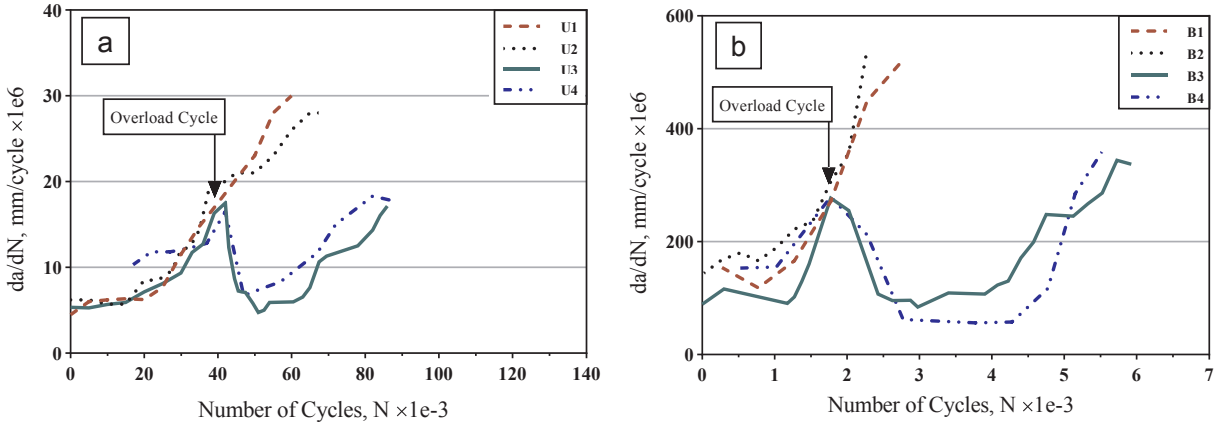

Fig. 8. Evolution of crack growth rate as a function of number of cycles for uniaxial (a) and biaxial (b) tests. Note that the axis with number of cycles, N, has been corrected so that all curves coincide in the overload cycle.

bottom) of the virtual extensometer points relative to the crack line. Such definition is based on the schematic in Fig. 10.

To determine the presence of crack closure, the COD was monitored in different stages of the test (i.e. before and after overload cycle). All COD measurements were derived from the external surface of the specimen. Since the specimen thickness in the crack region was small (2 mm), no large differences are expected across the thickness. Fig. 11 shows how the COD changes during a complete cycle for samples U3 and B3. A similar evolution was observed on samples U4 and B4. The large plasticity developed during the overload in sample U3 caused a shadow in the crack tip region that impeded using DIC during the cycle just after the overload. Accordingly, for sample U3, the second fatigue condition that was analysed was two cycles after applying the overload. It can be seen in Fig. 11 that the loading and unloading path in sample

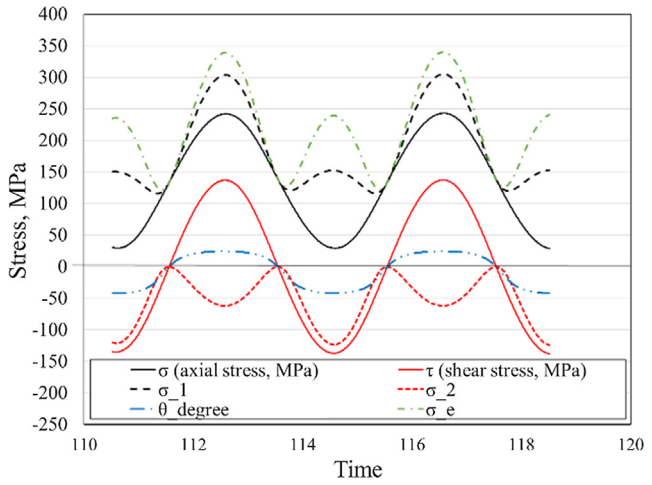

Fig. 9. Variation of nominal, principal and von Mises equivalent stresses and variation of the principal axis orientation during 2 complete cycles in samples B.

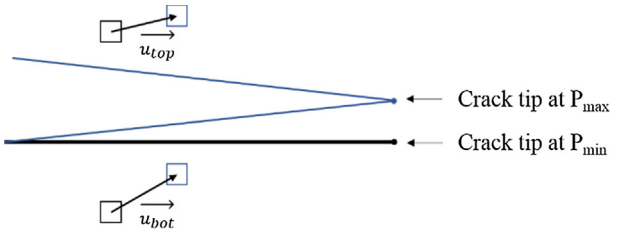

Fig. 10. Displacement vectors u_{top} and u_{bot} behind de crack tip.

B3 is considerably deviated from linear behaviour. In addition, right after overload cycle, the maximum value of COD for sample B3 has been reduced by 0.95 μm (18%), while it increases only by 0.1 μm for sample U3. On the other hand, from Fig. 11c and d, it can be observed that the slope of COD curve has been changed at lower portion of the graph by increasing the crack length for sample U3 which was under pure axial loading. This change in the slope is often referred to as "knee" [59].

A compliance based method [60] was followed to quantify the opening load. Fig. 12 shows the procedure to evaluate the opening load during the experiment. Fig. 12a and c show the compliance curve for samples U3 and B3, respectively. Similar evolution was observed on samples U4 and B4. In Fig. 12b, COD-offset refers to the distance between the fitted least squares line at loads higher than 8 kN (50% of loading range) and the COD curve at each point. The estimated opening load for sample U3 at crack lengths of 2.06, 2.38 and 3.04 mm was 3.47, 4.35 and 3.58 kN, respectively. The ratio opening load to maximum load, P_{op}/P_{max}, was 0.20, 0.25 and 0.21 for the three different crack lengths, respectively. The same procedure was followed for sample B3 (Fig. 12d) but the offset-compliance loops did not exhibit any closure before and after the overload cycle.

5.3. Experimental evaluation of SIF by DIC

DIC was employed to extract the displacement field around the crack tip. Following the method described previously [26,57], the stress intensity factor in mode I and mode II was estimated. The method includes fitting the experimental displacement data to Williams' power series using a multipoint over-deterministic method [24]. The hybrid experimental-analytical method has been successfully used to estimate the opening mode and shear mode stress intensity factors (K_I and K_{II})

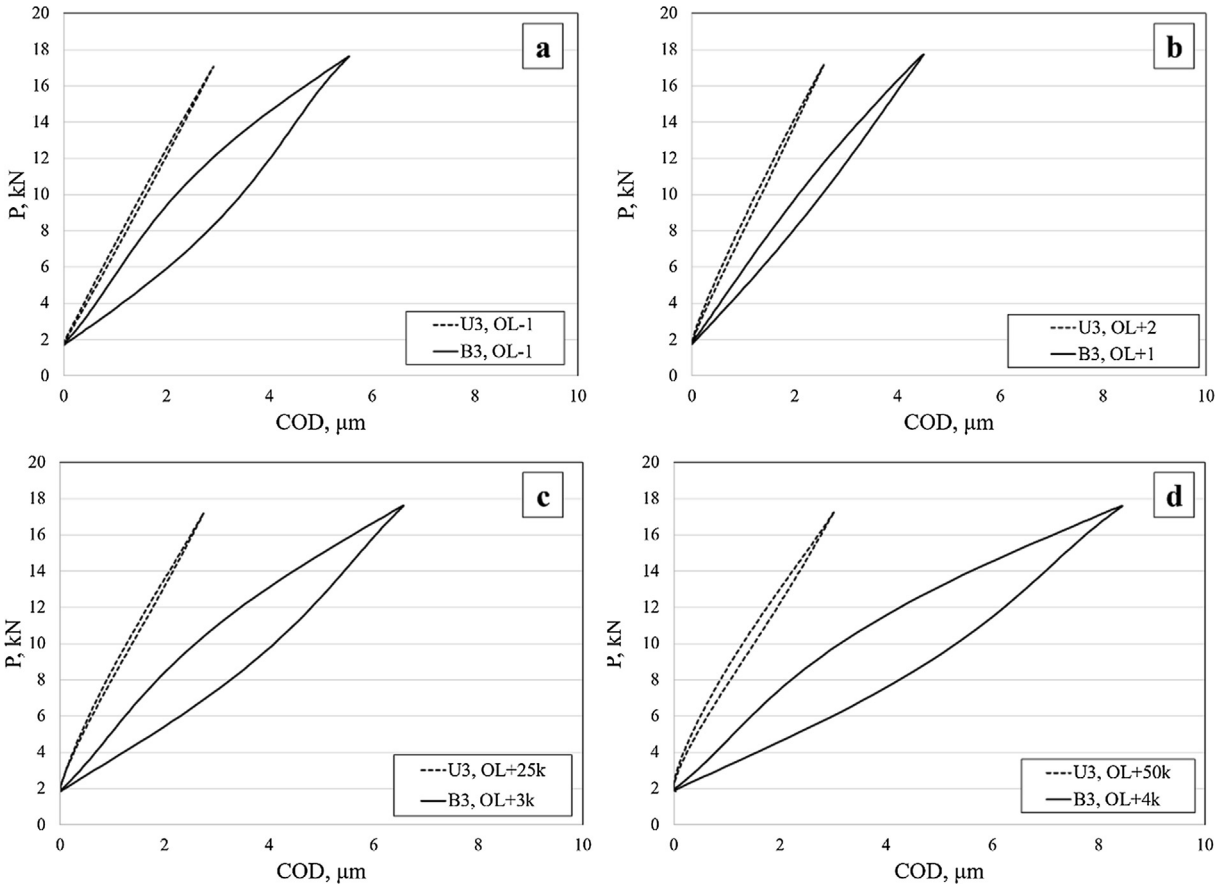

Fig. 11. COD behaviour for Sample 1 and Sample 2 at different stages of loading (different crack lengths).

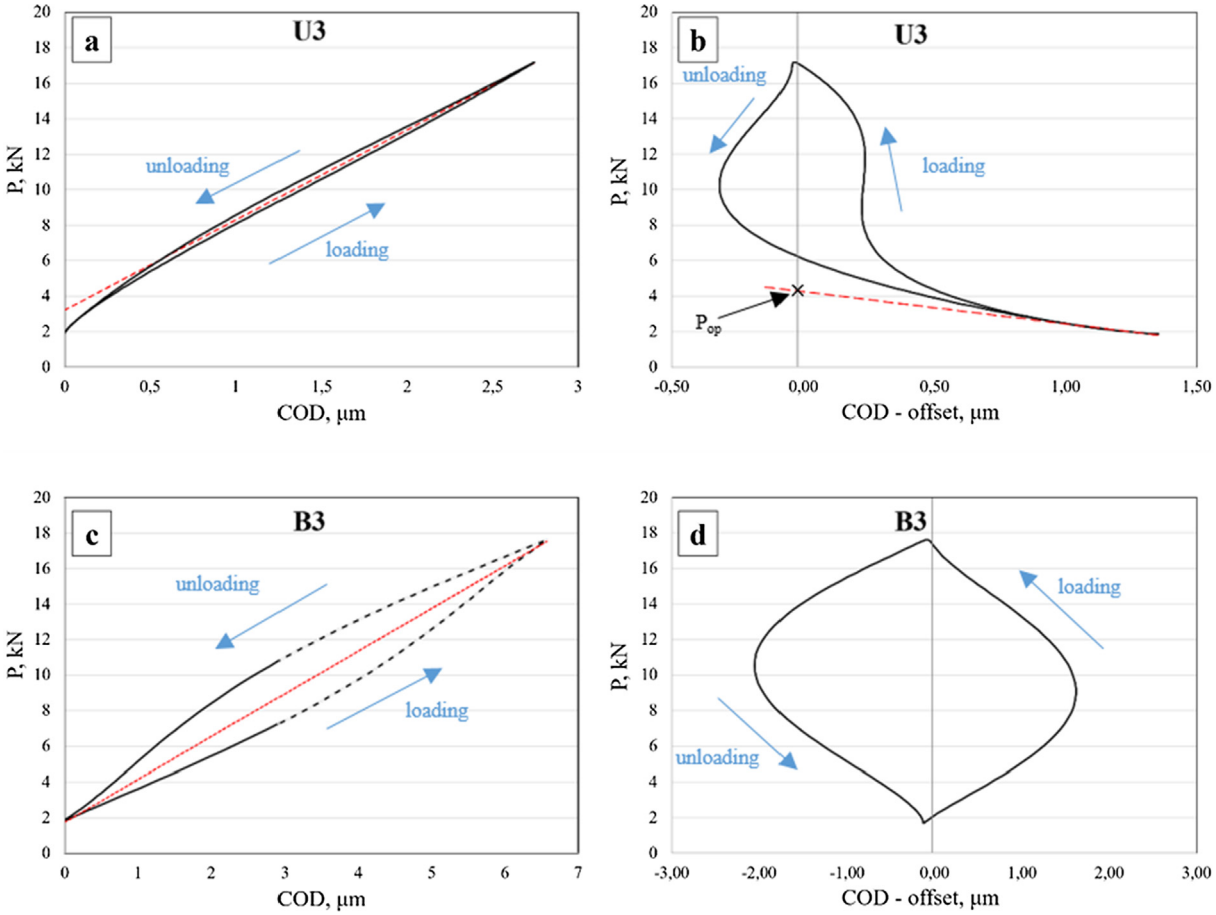

Fig. 12. Evaluation of opening load for sample U3 (a and b) and sample B3 (c and d) after overload at crack length of 2.39 and 2.42 mm, respectively.

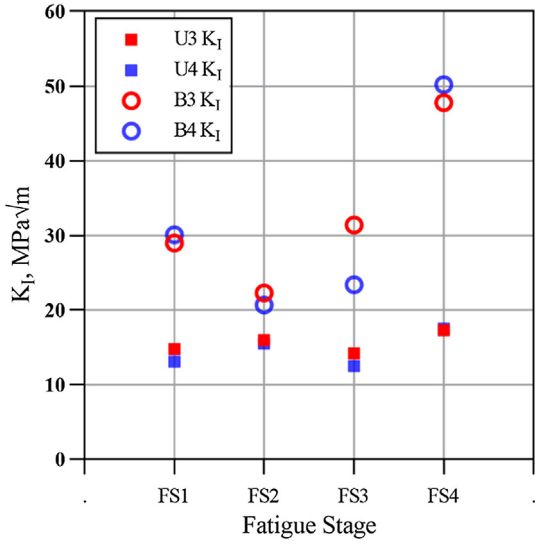

Fig. 13. Evolution of mode I stress intensity factor, ΔK_I, estimated by hybrid DIC based tool on samples U3, U4, B3 and B4 for the different fatigue stages defined in Table 7.

for different materials and geometries, with and without stress concentrators [57,61–64]. By taking into account the size of the area of interest ($0.8 \times 0.8\ mm^2$), two terms in the Williams' solution were used as suggested in [42]. Since the angle of crack propagation in the samples B was different to zero, the images were initially rotated so that the crack appeared horizontal in all images. This step was followed by the processing of the data to extract the vertical and the horizontal displacements with respect the axial loading axis. Fig. 4 illustrates this procedure for sample B3 with a crack length of 1.1 mm, as well as the crack-tip vertical displacement contour. Displacement data points inside an area of $0.8 \times 0.8\ mm^2$ were extracted and fitted to an analytical model. Williams' solution written in the form of Eqs. (5) and (6) was used to calculate SIFs.

$$u = \frac{K_I}{2\mu}\sqrt{\frac{r}{2\pi}}cos\frac{\theta}{2}\left(\kappa - 1 + 2sin^2\frac{\theta}{2}\right) + \frac{K_{II}}{2\mu}\sqrt{\frac{r}{2\pi}}sin\frac{\theta}{2}\left(\kappa + 1 + 2cos^2\frac{\theta}{2}\right) + \frac{T}{8\mu}r(\kappa+1)cos\theta + a_0 - Rsin(\theta) \quad (5)$$

$$v = \frac{K_I}{2\mu}\sqrt{\frac{r}{2\pi}}sin\frac{\theta}{2}\left(\kappa + 1 - 2cos^2\frac{\theta}{2}\right) + \frac{K_{II}}{2\mu}\sqrt{\frac{r}{2\pi}}cos\frac{\theta}{2}\left(\kappa - 1 - 2cos^2\frac{\theta}{2}\right) + \frac{T}{8\mu}r(\kappa-3)sin\theta + +b_0 + Rrcos(\theta) \quad (6)$$

where a_0 and b_0 account for the rigid body translation and R_0 is used to compensate for the rigid body rotation. The mixed-mode SIF were evaluated according to:

$$K_I = a_1\sqrt{2\pi} \qquad K_{II} = -b_1\sqrt{2\pi} \qquad T = 4a_2 \quad (7)$$

where K_I and K_{II} are the mode I and II of stress intensity factor, respectively, and T represents T-stress. Additional details about the hybrid methodology for extracting the SIF can be found elsewhere [26,42]. Figs. 13 and 14 show the opening mode stress intensity factor (ΔK_I) and the shear mode stress intensity factor (ΔK_{II}), respectively, as inferred with the hybrid methodology. Fig. 15 shows the evolution of

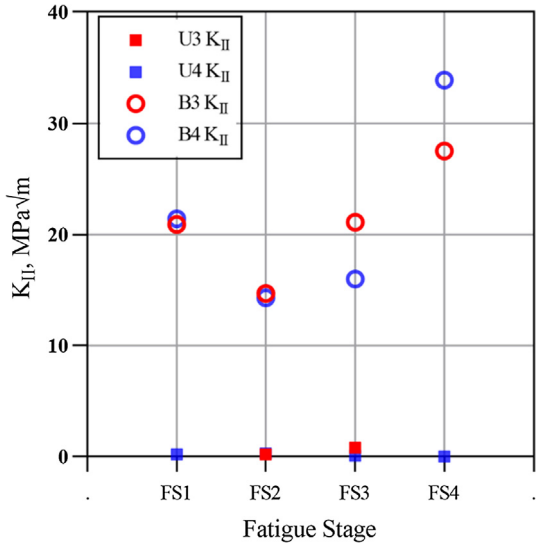

Fig. 14. Evolution of mode II stress intensity factor, ΔK_{II}, estimated by hybrid DIC based tool on samples U3, U4, B3 and B4 for the different fatigue stages defined in Table 7.

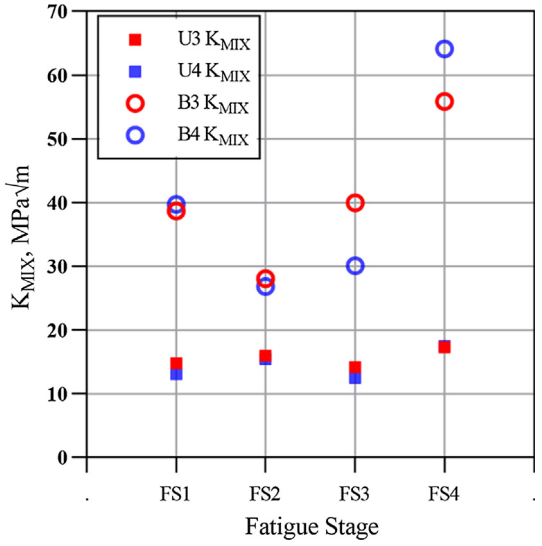

Fig. 15. Evolution of the combined stress intensity factor, ΔK_{MIX}, (Eq. (8)) estimated by hybrid DIC based tool on samples U3, U4, B3 and B4 for the different fatigue stages defined in Table 7.

the combined stress intensity factor where the influence of both mode I and mode II loadings is included [65]:

$$\Delta K_{MIX} = [\Delta K_I^4 + 8\Delta K_{II}^4]^{0.25} \quad (8)$$

The small values of ΔK_{II} compared to ΔK_I values for samples U throughout the entire test (Figs. 13 and 14) indicate that the crack in the uniaxial samples is predominantly subjected to opening mode loads. For the OL−1 and OL+50 k stages, a small negative ΔK_{II} value was detected, being indicative of a slight shear relative movement between the top and bottom crack faces in the opposite direction to the OL+2 and the OL+25 k stages. On the other hand, for the biaxial samples (Fig. 14), the ΔK_{II} is consistently larger (around 60% of the ΔK_I values), thus indicating a stronger shear mode component on the biaxial cracks. Such a stronger shear mode component might be related to crack flank jamming caused as the crack is loaded at a different direction to the displacements used in its growth [66].

6. Discussion

Fatemi-Socie critical plane model was used to predict the fatigue life of a S355 steel subjected to two different loading conditions, namely only uniaxial load and a combination of axial and torsional loads. Table 5 indicates that the critical plane method gives acceptable predictions for the fatigue life and these predictions are on the conservative side for the uniaxial samples. For the biaxial samples, the predictions are on the conservative side only for the overloaded cases (B3 and B4). The model also gives some information regarding the failure plane (Table 6) but the predictions are not very accurate probably due to the microstructure effect on the propagation plane [67]. The current critical plane method does not include any means for taking transient effects such as overload into account. Nevertheless they are useful to infer total fatigue life information. In addition, critical plane method requires the stress/strain values to be corrected to take into account stress concentration caused by a hole.

The damage tolerance approach based on DIC analysis of the surface allows a more detailed analysis of the transient effect to be performed and appears to be sensitive to closure mechanisms. Fig. 8 clearly shows the retardation effect produced by a 40% overload cycle. While non-overloaded samples (U1, U2, B1 and B2 in Fig. 8) show a continuously increasing evolution, overloaded samples (U3, U4, B3 and B4) clearly show a reduction in the fatigue crack growth rate after the overload cycle takes place. In addition, both the COD and SIF were larger for the biaxial samples than the uniaxial samples, thus indicating a higher damage in the biaxial samples and therefore a shorter fatigue life in samples B than in samples U (Fig. 8). In other words, the biaxial combination of loads produces a higher crack growth rate than the tensile loads. On the other hand, both COD and SIF approaches can capture the overload effect. Figs. 11, 13–15 show a decrease in the driving force related to the retardation period induced by the overload event. A similar transient was also observed under uniaxial loading, e.g. [68–70]. The closure retardation occurs as the crack grows through the compressive residual stress field created by the overload. The residual stress effect is measured in samples U3 and U4 as a reduction in the driving force and an increment in the opening load. The reduction in SIF following the overload observed in samples U3 and U4 appears to be in accordance with previous works [71,72] with smaller overload ratio inducing a smaller reduction of the driving force and therefore a shorter retardation period. The retardation in the crack propagation is longer in samples U3 and U4 than in samples B3 and B4. In addition, both the COD and SIF approaches agree well with the fatigue crack growth trend observed (Fig. 8). The decrease in COD and SIF following the overload cycle can be seen in samples U3 and U4 (Fig. 8.a) and samples B3 and B4 (Fig. 8.b) as a decrease in da/dN. For samples U3 and U4, by the end of the experiment, the crack growth rate returns to the pre-overload values ($\sim 18 \times 10^{-6}$ mm/cycle) and the COD and SIF also reach pre-overload values. For samples B3 and B4, the retardation effect is much shorter ($\sim$3500 cycles for samples B3 and B4 versus $\sim$44,000 cycles in samples U3 and U4) and this is also clear in the evolution of both the COD and SIF. This agreement indicates that SIF values derived from the crack tip field are effective and can be used to model transient conditions, in agreement with previous studies [25,61,73]. Moreover, the COD measurement allowed compliance offset technique to be applied for the uniaxial samples. The increase in the opening load 25,000 cycles after the overload in samples U3 was in line with the retardation observed (Fig. 8a). However, it was not possible to apply the compliance offset technique to estimate the opening load under biaxial loading. The SIF approach allowed quantifying the level of mixed mode on all the samples. Almost no ΔK_{II} was measured on the uniaxial samples (Fig. 14) because only uniaxial load was applied and the crack grew perpendicular to the load direction. For the biaxial samples, B3 and B4, the combination of axial and torsional loads and the large difference in cracking angle on both sides of the hole (Table 6) promoted shear mode loading on the crack. Such a shear

mode component was captured by the SIF approach throughout the entire test (Fig. 14), with a $\Delta K_{II}/\Delta K_I$ average ratio of 0.66 and 0.69 throughout the test for samples B3 and B4, respectively. Accordingly, the overload in samples B3 and B4 was introduced under mixed-mode conditions, unlike for samples U3 and U4 where a pure mode I overload was applied. The mechanisms induced under a mixed-mode overload are different to those under mode I overloads, with shear crack and cavities having a predominant role [74] and less of a blunting effect at the crack tip under a mixed mode overload [31]. The result is a smaller transient effect in the mixed-mode case (samples B3 and B4) than in the mode I case (samples U3 and U4), suggesting a stronger presence of crack closure under uniaxial loading than under biaxial loading. The acceleration often exhibited right after the overload event [75,76] is captured clearly by the SIF approach in the uniaxial samples, U3 and U4 (Figs. 13 and 15). The biaxial samples, B3 and B4 do not show such acceleration after the overload cycle (Figs. 13 and 15). This is consistent with a more severe blunting being introduced on a pure more I crack than on a mixed mode (I + II) crack, which in turn reduces the closure effect existing before the overload was introduced [75]. Such closure reduction is probably causing the crack advance acceleration immediately following the overload in samples U3 and U4.

7. Conclusions

This work set out to characterise the fatigue behaviour of S355 structural steel under uniaxial and biaxial loads and to examine the differences caused by a 40% overload cycle under both types of loads. The investigation is based on different tools, namely Fatemi-Socie critical plane method and damage tolerant approach analysis via COD and SIF. Fatemi-Socie has been used to estimate approximately the fatigue life of the material and has been very useful to quantify the differences between the two types of loads in combination with a stress raiser. Fatemi-Socie model has been able to quantify the reduction in fatigue life caused by shifting from only axial load to a combination of axial and torsional loads. The current implementation of Fatemi-Socie did not allow to take transient crack growth effect caused by the overload into consideration. Damage tolerant analysis based on DIC technique has shown an increase in crack growth rate by a factor of about 20 when in-phase torsional load is added in-phase to the uniaxial load. The retardation caused by the overload has been captured accurately both by COD and SIF derived by DIC technique. The extent of the retardation has been shown to be much shorter when torsional and axial loads act simultaneously than when only axial load is applied, even though the same overload ratio was introduced under both types of load. For the uniaxial overload, the retardation effect has been ascribed to closure mechanisms that induce a reduction in the driving force (COD and SIF) which manifests as a premature contact between the crack faces throughout the extension of the overload plastic zone. The estimation of the SIF also allowed the mode mixity (I + II) to be quantified. The mode II SIF was on average around 33% smaller than the mode I SIF during the biaxial tests. The overload in the biaxial samples has then been identified as a mixed-mode type overload (as opposed to a pure mode I overload applied to the uniaxial sample). The smaller retardation effect for the biaxial loading has been linked to a drastic reduction in the crack closure effect and the activation of different shear mechanisms. It has been possible to apply the compliance offset method from DIC data for the estimation of the opening load in the cylindrical specimen studied but only under uniaxial load. The compliance measurements obtained under biaxial load did not allow the compliance offset method to generate opening load estimations under biaxial load.

Declaration of Competing Interest

The authors declare that they have no known competing financial interests or personal relationships that could have appeared to influence the work reported in this paper.

Acknowledgements

Financial support of Ministerio de Economia y Competitividad through grant reference MAT2016-76951-C2-2-P is greatly acknowledged. Support from the Oceanic Engineering Research Institute from Malaga is also acknowledged.

References

[1] Meggiolaro MA, De Castro JTP. Fatigue design techniques. Low-cycle and multiaxial fatigue, vol. II, 1st ed. Platform, C.I.P.
[2] Hashin Z. Fatigue failure criteria for combined cyclic stress. Int J Fract 1981;17:101–9.
[3] Sonsino CM, Grubisic V. Fatigue behaviour of cyclically softening and hardening steels under multiaxial elastic-plastic deformation, vol. 853; 1985.
[4] Fatemi A, Socie DF. A critical plane approach to multiaxial fatigue damage including out-of-phase loading. Fatigue Fract Eng Mater Struct 1988;11:149–65.
[5] Garud Y. Multiaxial fatigue: a survey of the state of the art. J Test Eval ASTM 1981;9.
[6] Ellyin F, Golos K. Multiaxial fatigue damage criterion. J Eng Mater Technol 1988;110:63–8.
[7] Irwin G. Analysis of stresses and strains near the end of a crack traversing a plate. J Appl Mech 1957;24:361–4.
[8] Paris P, Erdogan J. Critical analysis of crack growth propagation laws. J Basic Eng 1963;85D:528–34.
[9] Anderson TL. Fracture mechanics: fundamentals and applications. 3rd ed. CRC Press, Taylor & Francis Group; 2005.
[10] deMatos PFP, Nowell D. Numerical simulation of plasticity-induced fatigue crack closure with emphasis on the crack growth scheme: 2D and 3D analyses. Eng Fract Mech 2008;75:2087–114.
[11] Sutton MA, Orteu JJ, Schreier H. Image correlation for shape, motion and deformation measurements: basic concepts, theory and applications. Springer Science & Business Media; 2009.
[12] Nowell D, Paynter RJH, De-Matos PFP. Optical methods for measurement of fatigue crack closure: moiré interferometry and digital image correlation. Fatigue Fract Eng Mater Struct 2010;33:778–90.
[13] Westergaard HM. Bearing pressures and cracks. J Appl Mech 1939;61.
[14] Williams ML. On the stress distribution at the base of a stationary crack. J Appl Mech 1957;24:109–14.
[15] Muskhelishvili NI. Some basic problems of the mathematical theory of elasticity. Groningen, Holland: P. Noordhoff Ltd.:; 1953.
[16] Christopher CJ, James MN, Patterson EA, Tee KF. Towards a new model of crack tip stress fields. Int J Fract 2007;148:361–71.
[17] Ramesh K, Gupta S, Kelkar AA. Evaluation of stress field parameters in fracture mechanics by photoelasticity—revisited. Eng Fract Mech 1997;56:25–45.
[18] Diaz FA, Patterson EA, Tomlinson RA, Yates JR. Measuring stress intensity factors during fatigue crack growth using thermoelasticity. Fatigue Fract Eng Mater Struct 2004;27:571–83.
[19] McNeill SR, Peters WH, Sutton MA. Estimation of stress intensity factor by digital image correlation. Eng Fract Mech 1987;28:101–12.
[20] Lopez-Crespo P, Peralta JV, Withers PJ. Synchrotron X-ray diffraction based method for stress intensity factor evaluation in the bulk of materials. Theor Appl Fract Mech 2018;98:72–7.
[21] Yoneyama S, Kitagawa A, Iwata S, Tani K, Kikuta H. Bridge deflection measurement using digital image correlation. Exp Tech 2007;31:34–40.
[22] Sutton MA, Li N, Joy DC, Reynolds AP, Li X. Scanning electron microscopy for quantitative small and large deformation measurements Part I: SEM imaging at magnifications from 200 to 10,000. Exp Mech 2007;47:775–87.
[23] Carroll JD, Abuzaid W, Lambros J, Sehitoglu H. High resolution digital image correlation measurements of strain accumulation in fatigue crack growth. Int J Fatigue 2013;557:140–50.
[24] Sanford RJ, Dally JW. A general method for determining mixed-mode stress intensity factors from isochromatic fringe patterns. Eng Fract Mech 1979;11:621–33.
[25] Yoneyama S, Ogawa T, Kobayashi Y. Evaluating mixed-mode stress intensity factors from full-field displacement fields obtained by optical methods. Eng Fract Mech 2007;74:1399–412.
[26] Yates JR, Zanganeh M, Tai YH. Quantifying crack tip displacement fields with DIC. Eng Fract Mech 2010;77:2063–76.
[27] Carlson RL, Kardomateas GA, Bates PR. The effects of overloads in fatigue crack growth. Int J Fatigue 1991;13:453–60.
[28] Salvati E, O'Connor S, Sui T, Nowell D, Korsunsky AM. A study of overload effect on fatigue crack propagation using EBSD, FIB–DIC and FEM methods. Eng Fract Mech 2016;167:210–23.
[29] deMatos PFP, Nowell D. Experimental and numerical investigation of thickness effects in plasticity-induced fatigue crack closure. Int J Fatigue 2009;31:1795–804.
[30] Yusof F, Lopez-Crespo P, Withers PJ. Effect of overload on crack closure in thick and thin specimens via digital image correlation. Int J Fatigue 2013;56:17–24.
[31] Srinivas V, Vasudevan P. Study of the influence of mixed mode overload on mode I fatigue crack propagation. Int J Press Vessels Pip 1993;56:409–17.
[32] Sander M, Richard HA. Finite element analysis of fatigue crack growth with interspersed mode I and mixed mode overloads. Int J Fatigue 2005;27:905–13.
[33] Sander M, Richard HA. Experimental and numerical investigations on the influence of the loading direction on the fatigue crack growth. Int J Fatigue 2006;28:583–91.

[34] Socie DF, Marquis GB. Multiaxial fatigue. Warrendale, PA (USA): Society of Automotive Engineers, Inc.; 2000.
[35] Chaves V. Ecological criteria for the selection of materials in fatigue. Fatigue Fract Eng Mater Struct 2014;37:1034–42.
[36] Suresh S. Fatigue of materials. Cambridge: Cambridge University Press; 2004.
[37] ASTM E647-15. Standard test method for measurement of fatigue crack growth rates. West Conshohocken, PA; 2015 [ISBN 5967164006].
[38] Lopez-Crespo P, Moreno B, Lopez-Moreno A, Zapatero J. Characterisation of crack-tip fields in biaxial fatigue based on high-magnification image correlation and electro-spray technique. Int J Fatigue 2015;71:17–25.
[39] Zanganeh M, Lopez-Crespo P, Tai YH, Yates JR. Locating the crack tip using displacement field data: a comparative study. Strain 2013;49:102–15.
[40] Documents R. ASTM E647-00: standard test method for measurement of fatigue crack growth rates. American Society of Testing and Materials, Annual Book of Standards, vol. 03; 1999.
[41] Vic-2D V6 Reference Manual. Correlated Solutions Incorporated (C.S.Inc).
[42] Mokhtarishirazabad M, Lopez-Crespo P, Moreno B, Lopez-Moreno A, Zanganeh M. Evaluation of crack-tip fields from DIC data: a parametric study. Int J Fatigue 2016;89:11–9.
[43] Karolczuk A, Macha E. A review of critical plane orientations in multiaxial fatigue failure criteria of metallic materials. Int J Fract 2005;134:267–304.
[44] Lopez-Crespo P, Moreno B, Lopez-Moreno A, Zapatero J. Study of crack orientation and fatigue life prediction in biaxial fatigue with critical plane models. Eng Fract Mech 2015;136:115–30.
[45] Systems, S.A. ANSYS; 1996.
[46] Chaboche JL. Constitutive equations for cyclic plasticity. Int J Plast 1989;5:247–302.
[47] Halama R, Sedlák J, Fusek M, Poruba Z. Uniaxial and biaxial ratcheting of ST52 steel under variable amplitude loading-experiments and modeling. Proc Eng 2015;101:185–93.
[48] Itoh T, Sakane M, Ohnami M, Socie DF. Nonproportional low-cycle fatigue criterion for type 304 stainless steel. J Eng Mater Technol-Trans ASME 1995;117:285–92.
[49] Itoh T, Nakata T, Sakane M, Ohnami M. Nonproportional low cycle fatigue of 6061 aluminum alloy under 14 strain paths. Eur Struct Integr Soc 1999;25:41–54.
[50] Liu Y, Mahadevan S. Multiaxial high-cycle fatigue criterion and life prediction for metals. Int J Fatigue 2005;27:790–800.
[51] Erickson M, Kallmeyer AR, Van Stone RH, Kurath P. Development of a multiaxial fatigue damage model for high strength alloys using a critical plane methodology. J Eng Mater Technol 2008;130:041008.
[52] Han C, Chen X, Kim KS. Evaluation of mutiaxial fatigue criteria under irregular loading. Int J Fatigue 2002;24:913–22.
[53] Llano-Vizcaya LDel, Rubio-Gonzalez C, Mesmacque G, Cervantes-Hernandez T. Multiaxial fatigue and failure analysis of helical compression springs. Eng Failure Anal 2006;13:1303–13.
[54] Image J.
[55] Reis L, Freitas MJ. Crack initiation and growth path under multiaxial fatigue loading in structural steels. Int J Fatigue 2009;31:1660–8.
[56] Gates NR, Fatemi A. Multiaxial variable amplitude fatigue life analysis using the critical plane approach, Part II: notched specimen experiments and life estimations. Int J Fatigue 2018;106:56–69.
[57] Mokhtarishirazabad M, Lopez-Crespo P, Moreno B, Lopez-Moreno A, Zanganeh M. Optical and analytical investigation of overloads in biaxial fatigue cracks. Int J Fatigue 2017;100(part 2):583–90.
[58] Stephens R, Fatemi A, Stephens RR, Fuchs H. Metal fatigue in engineering. 2nd ed. Wiley-Interscience; 2001.
[59] Joyce JA, Sutton GE. An automated method of computered-controlled low-cycle fatigue crack growth testing using the eslastic-plastic parameter cyclic. In: Cullen WH, Landgraf RW, Kaizand LR, Underwood JH, editors. Automated tests methods for fracture and fatigue crack growth, ASTM STP 877. 1985. p. 227–47.
[60] Skorupa M, Baretta S, Carboni M, Machiniewicz T. An algorithm for evaluating crack closure from local compliance measurements. Fatigue Fract Eng Mater Struct 2002;25:261–73.
[61] Lopez-Crespo P, Shterenlikht A, Patterson EA, Withers PJ, Yates JR. The stress intensity of mixed mode cracks determined by digital image correlation. J Strain Anal Eng Des 2008;43:769–80.
[62] López-Crespo P, Burguete RL, Patterson EA, Shterenlikht A, Withers PJ, Yates JR. Study of a crack at a fastener hole by digital image correlation. Exp Mech 2009;49.
[63] Lopez-Crespo P, Shterenlikht A, Yates JR, Patterson EA, Withers PJ. Some experimental observations on crack closure and crack-tip plasticity. Fatigue Fract Eng Mater Struct 2009;32:418–29.
[64] Mokhtarishirazabad M, Lopez-Crespo P, Zanganeh M. Stress intensity factor monitoring under cyclic loading by digital image correlation. Fatigue Fract Eng Mater Struct 2018;41:2162–71.
[65] Tanaka K. Fatigue crack propagation from a crack inclined to the cyclic tensile axis. Eng Fract Mech 1974;6:493–507.
[66] Tong J, Yates JR, Brown MW. A model for sliding mode crack closure. Parts I and II. Eng Fract Mech 1995;52:599–623.
[67] Reis L, Li B, Leite M, Freitas MJ. Effects of non-proportional loading paths on the orientation of fatigue crack path. Fatigue Fract Eng Mater Struct 2005;28:445–54.
[68] Yisheng W, Schijve J. Fatigue crack closure measurements on 2024–T3 sheet specimens. Fatigue Fract Eng Mater Struct 1995;18:917–21.
[69] Nowell D, De-Matos PFP. Application of digital image correlation to the investigation of crack closure following overloads. Proc Eng 2010;2:1035–43.
[70] Nowell D, Kartal ME, deMatos PFP. Digital image correlation measurement of near-tip fatigue crack displacement fields: constant amplitude loading and load history effects. Fatigue Fract Eng Mater Struct 2013;36:3–13.
[71] Nganga SP, James MN. Variable amplitude loading in en8 (080m40) steel: a detailed experimental study of crack growth. Fatigue Fract Eng Mater Struct 1996;19:207–16.
[72] Meggiolaro MA, de Castro JTP. On the dominant role of crack closure on fatigue crack growth modeling. Int J Fatigue 2003;25:843–54.
[73] Vasco-Olmo JM, Díaz FA, García-Collado A, Dorado-Vicente R. Experimental evaluation of crack shielding during fatigue crack growth using digital image correlation. Fatigue Fract Eng Mater Struct 2015;38:223–37.
[74] Nayeb-Hashemi H, Taslim ME. Effects of the transient mode II on the steady state crack growth in mode I. Eng Fract Mech 1987;26:789–807.
[75] Corbly DM, Packman PF. On the influence of single and multiple peak overloads on fatigue crack propagation in 7075–T6511 aluminum. Eng Fract Mech 1973;5:479–97.
[76] Wheatley G, Hu XZ, Estrin Y. Effects of a single tensile overload on fatigue crack growth in a 316L steel. Fatigue Fract Eng Mater Struct 1999;22:1041–51.